Supplementary Material for Foveated AR: Dynamically-Foveated Augmented Reality Display

JONGHYUN KIM, YOUNGMO JEONG*, MICHAEL STENGEL, KAAN AKŞIT, RACHEL ALBERT, BEN BOUDAOUD, TREY GREER, JOOHWAN KIM, WARD LOPES, ZANDER MAJERCIK, PETER SHIRLEY, JOSEF SPJUT, MORGAN MCGUIRE, and DAVID LUEBKE, NVIDIA, United States

ACM Reference Format:
Jonghyun Kim, Youngmo Jeong, Michael Stengel, Kaan Akşit, Rachel Albert, Ben Boudaoud, Trey Greer, Joohwan Kim, Ward Lopes, Zander Majercik, Peter Shirley, Josef Spjut, Morgan McGuire, and David Luebke. 2019. Supplementary Material for Foveated AR: Dynamically-Foveated Augmented Reality Display. *ACM Trans. Graph.* 38, 4, Article 99 (April 2019), 22 pages. https://doi.org/10.1145/nnnnnnn.nnnnnnn

A DETAILED ANALYSIS OF FOVEATED DISPLAY

A.1 Holographic Optical Element Simulator

In this section, we present our numerical simulation method for Holographic Optical Elements (HOEs). Like much work on displays adopting HOEs, Kogelnik's [1969] coupled-wave theory provides a theoretical background for volume grating-based holograms. A fully recorded HOE can be modeled as a periodic volume grating, which makes use of strong resonant diffraction known as Bragg diffraction. If the thickness of the grating structure is sufficiently large at the molecular level, all orders of the diffracted beam can be eliminated with the exception of a single order with strong selectivity to Bragg matched light. With this knowledge of volume gratings, an HOE can be described as a group of planar gratings of infinitesimal lateral size in space. By modeling this optical element in tools such as Matlab and Zemax, ray tracing-based simulation with diffractive element can provide precise and straightforward results for both peripheral display performance and beam shaping experiments.

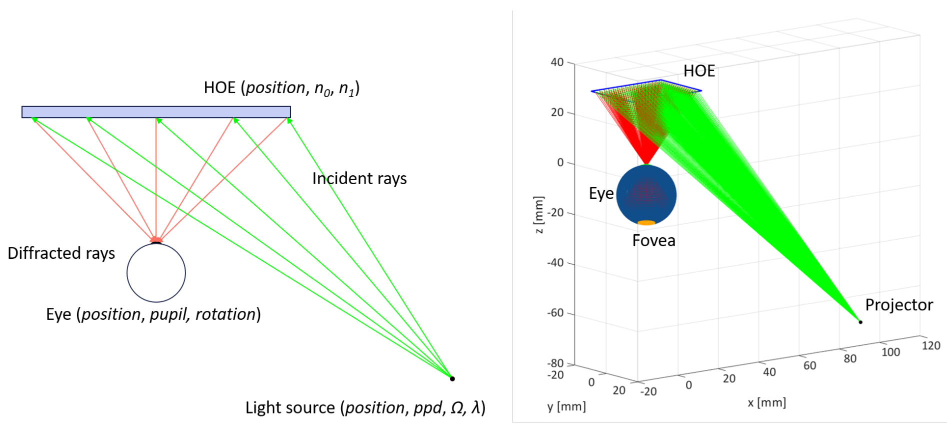

Fig. S1. (left) The schematic diagram of the HOE simulator for display parameters of the peripheral display and (right) three-dimensional visualization of the HOE simulator.

Figure S1 shows the schematic diagram of our HOE simulator and essential elements for the display. Each optical element, including the user/viewer has several parameters. For example position, size, thickness of the photopolymer, average refractive index (n_0), and refractive

*Also with Seoul National University.

Authors' address: Jonghyun Kim, jonghyunk@nvidia.com; Youngmo Jeong, youngmo.snu@gmail.com; Michael Stengel, mstengel@nvidia.com; Kaan Akşit, kaksit@nvidia.com; Rachel Albert, ralbert@nvidia.com; Ben Boudaoud, bboudaoud@nvidia.com; Trey Greer, tgreer@nvidia.com; Joohwan Kim, sckim@nvidia.com; Ward Lopes, wlopes@nvidia.com; Zander Majercik, amajercik@nvidia.com; Peter Shirley, pshirley@nvidia.com; Josef Spjut, jspjut@nvidia.com; Morgan McGuire, mcguire@nvidia.com; David Luebke, dluebke@nvidia.com, NVIDIA, 2788 San Tomas Expressway, Santa Clara, CA, United States, 95051.

0730-0301/2019/4-ART99 $15.00
https://doi.org/10.1145/nnnnnnn.nnnnnnn

index modulation strength (n_1) should be a group of parameters for an HOE. By setting these parameters close to their actual values, simulation results can adequately reflect the characteristics of a real HOE. The light source for a reference beam and diffracted rays for a signal beam are also defined. According to the parameters of the light source, including its position, resolution (in pixel per degree or PPD), viewing angle (Ω), and wavelength (λ), a bundle of rays are projected with unique k-vectors from the source to the HOE. Likewise, signal k-vectors can be defined from the points at which these rays hit the HOE to a point defined by the user. In our design, these diffracted rays focus at the center point of the pupil of the viewer since a Maxwellian view is intended from this location. After defining the pointwise signal and reference rays on the HOE, we can calculate and visualize how the recorded HOE functions when an arbitrary probe beam illuminates it. The main outputs of the simulator are a diffraction efficiency and diffracted direction for reconstructed rays. Using this simulator most of the HOE-based peripheral display characteristics can be analyzed including eye box, eye relief, pupil size, impact of rotation of the eye, differences of wavelengths, shrinkage of a photopolymer, and motion of HOEs.

Figure S2 demonstrates the concept of creating a dynamic eye box by laterally translating the HOE, which can be simulated using the HOE simulator. Note that the k-vectors in left figure have the same length on the k-space as shown in the right figure.**A** and **B** are regions on the HOE which have different grating vectors ($\overrightarrow{K_A}$, $\overrightarrow{K_B}$). Let's suppose the region $\boldsymbol{A}$ moves to x_2 on the $\overrightarrow{K_A}$ vector. If the $\overrightarrow{K_A}$ vector is illuminated by the reference beam for region $\boldsymbol{B}$ ($\overrightarrow{k_{r,s}}$), then the diffracted beam is tilted in the direction that the HOE moves. Using this property, we can achieve a larger dynamic eye box by translating the HOE according to the eye location from the gaze tracking input. Since the probe beam after the movement is different from the original reference beam, the Bragg match condition is no longer satisfied. The beta value method by Uchida can be used to model this Bragg mismatched condition, which introduces "grating vector cloud" along the z-axis [Uchida 1973].

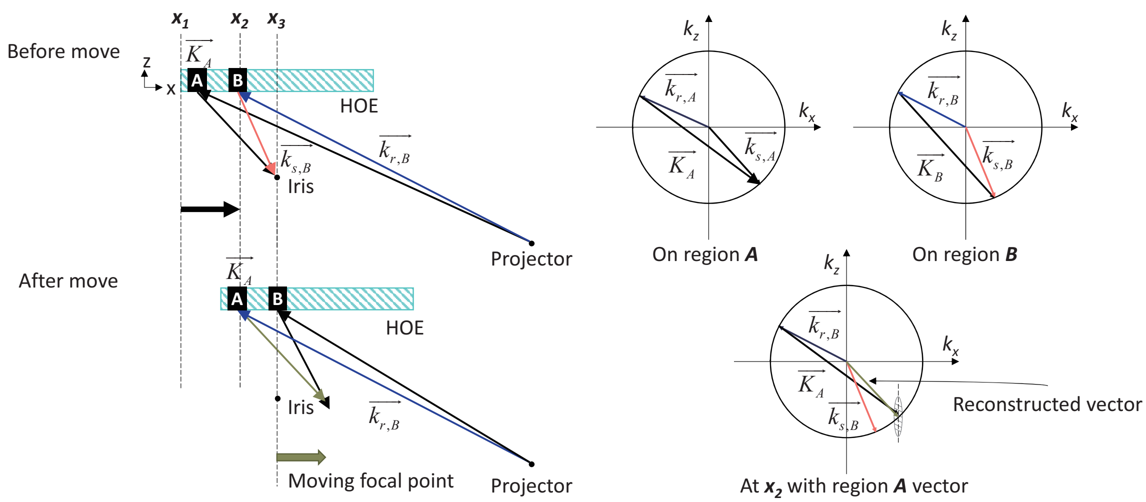

Fig. S2. (left) Dynamic eyebox by using moving HOE. (right) k-space diagram for moving HOE.

A.2 Beam Shaping and Optimization for Peripheral Display

A.2.1 Beam Width of a Laser Projector.

In our display system, the HOEs (one per eye) operate as concave mirrors that focus on-axis for off-axis laser light sources. To project the peripheral display to the retina via a Maxwellian view the HOEs should focus all reflected light at the center of the human pupil. The distance from the projector to the HOE can be adjusted within the allowable form factor of the system. If the minimum throw distance of the projector is decreased, a shorter focal length convex lens is needed to project a sharp image onto the HOE's surface. This procedure is referred to as *beam shaping*, which implies changing the optimal throw distance of a projector by inserting a lens in front of the projector. Using a short focal length lens can make the overall size of the system smaller but has the disadvantage that projected images may suffer from lens distortion and small depth of field. On the other hand, if the throw distance needs to be increased, the focal length of the beam shaping lens increases and the image can be stably projected on an off-axis HOE plane. However, the resolution of the display may be reduced as the available display area is limited by the size of the HOE.

To determine the optimal focal length, position, and direction of the beam shaping lens through simulation, the beam properties of the laser projector were investigated and recorded. The full color, laser scanning projector used in this work combines five different laser wavelengths to create a color beam (for speckle reduction when projecting on diffuse surfaces) and scans out pixels (over time) in a raster pattern using a resonant bi-axial MEMS scanning mirror. Initially, because collimated lasers are used as the light source for the projector, we assumed that pixel propagation could be modeled as a Gaussian beam. However, through experiments in which only one pixel of the projector's output is lit, it has been found that the divergence of a pixel with respect to distance is substantially different than when modeled as a Gaussian beam. Each pixel of the laser scanning projector reaches a beam waist within a short distance and then evolves linearly with the propagation distance as shown in Fig. S3. This was likely done as it allows "always in focus" performance across a wide range of projection throws without a need for a focus tuning element. From the trend line after the beam waist position, each pixel can be modeled in ray tracing software as a diverging beam. As shown in the left Fig. S3, each pixel has an elliptical shape, especially around exit pupil of the projector, which then spreads out towards a circle at a distance. This may be related to the resonant/raster scan operation of the MEMS mirror as the beam velocity (in the horizontal direction) follows a sinusoidal pattern, which when illuminated with a constant period color pattern, creates "shorter" pixels at the edges and "longer" pixels in the middle of the display.

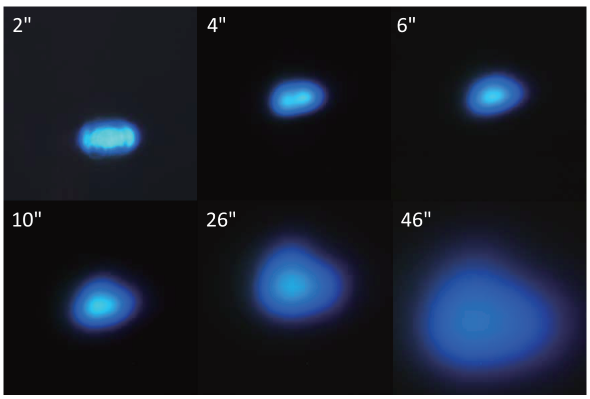

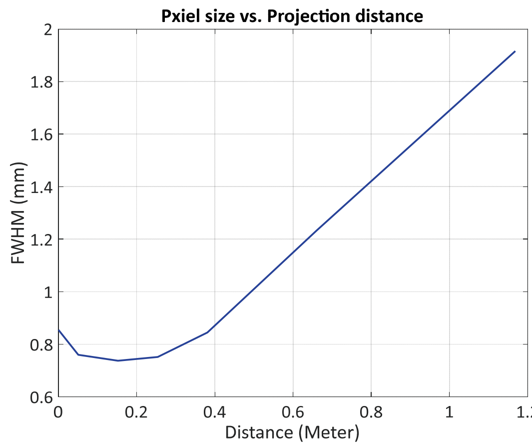

Fig. S3. (left) Shape of a pixel from the laser scanning projector across various projection throw distances (in inches). (right) Full Width Half Maximum (FWHM) of the pixels across various distances. The beam width increases linearly after the beam waist around 0.15 m.

A.2.2 Peripheral Display Optimization with Ray Tracing Software.

Ray tracing software is used to model light sources with the beam characteristics described above and search for beam shaping conditions that can project the sharpest image onto the HOE's surface. Based on a study of the divergence angle of the projector, each pixel is simulated as a light source having a specific size and diverging at a constant rate along the throw distance. Also, as with the HOE simulator, a surface that operates as a volume grating of a specific thickness is defined in the ray tracer. As mentioned above, the optimal focal length of the beam shaping lens is related to the resolution and depth of field of the display. The position and orientation of the lens are also adjusted to obtain uniform beam shaping results over the entire HOE to obtain a similar effect to lens rotation according to the Scheimpflug principle. In order to perform beam shaping with a commercially-available convex lens, several candidate lenses were selected and optimized for their locations and orientations. Zemax OpticStudio was used as the ray tracing software. After setting up the focal length, position, and orientation of the convex lens as optimization variables and minimizing Root-Mean-Square (RMS) spot size of pixels on the HOE as the objective function, a beam shaping optimization was performed. As a result of this optimization, we are able to improve the sharpness of the image by 14%.

Beam shaping lenses (as described above) can effectively reduce the size of each pixel reaching the eye. However, making the size of the pixels reaching the HOE plane uniform is desirable and imposes challenges all its own. Because we chose to use a commercially available convex lens in this work, it is not possible to modify the optical path as intended for all of the pixels spatially distributed across the HOE's surface. These limitations can be overcome by designing a freeform lens custom fit for the application. Unlike conventional convex/spheric lenses, a freeform surface is optimized for maximum performance given the designer's intent and can be designed directly using ray tracing software. Freeform surfaces can be used in lenses, mirrors, or a parts of a prism and are beginning to see more widespread adoption in AR devices [Huang and Hua 2018].

A.3 Calculation of Eye Box and Travel Distance in Peripheral Display

Using the HOE simulator introduced in the Section A.1, the required travel distance of the HOE at a given gaze angle can be calculated. Figure S5 shows simulation results for required HOE travel distance and resulting eye box. When the gaze angle changes, the eye rotates and the pupil center moves along a circular path accordingly. In the simulation, pupil aperture and eye ball diameter are set to 5 mm and 23 mm,

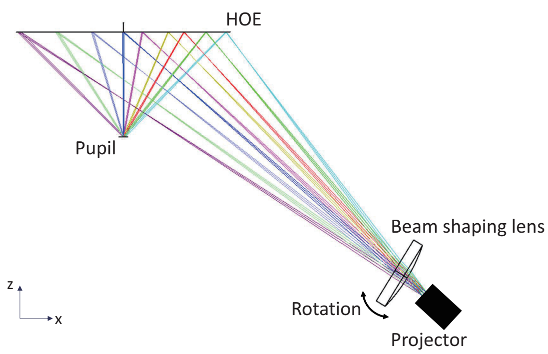

Fig. S4. Three-dimension layout of the peripheral display and beam shaping lens in Zemax OpticStudio. The position and rotation angle of the beam shaping lens are variable for the optimization.

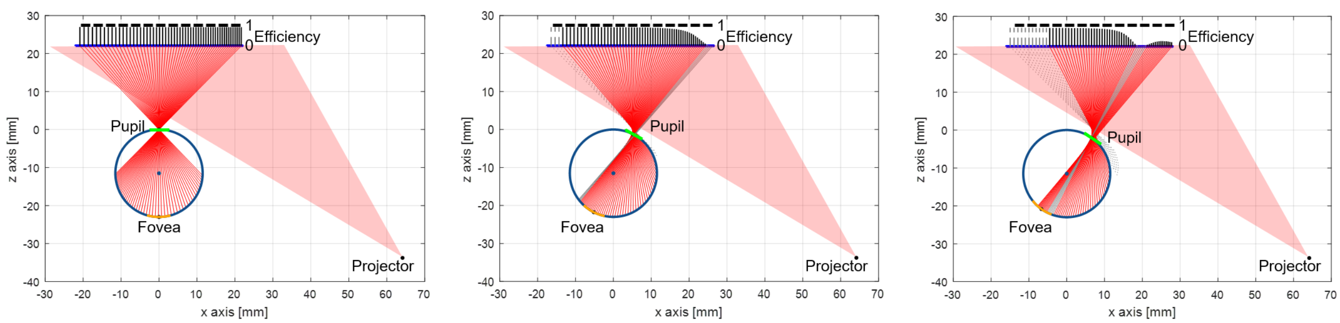

Fig. S5. The required HOE travel distance x_p and eye box simulation. The green line represents the pupil and the orange line is foveal region of the retina. The small lines on the top of each point on the HOE indicate the diffraction efficiency for the corresponding incident ray from the projector. (left) at the center (α = 0°, x_p = 0 mm, and FOV = 90.0°), (center) at the right most border of the eye box (α = 26.7°. x_p = 4.5 mm, and FOV = 90.3°), and (right) at the outside of the eye box (α = 35.7°, x_p = 6 mm, and FOV = 77.4°). Note that the gray lines indicate low efficiency rays (efficiency < 0.1) and the dotted lines are the rays cannot go into the pupil.

respectively. We then sweep the HOE in the lateral direction to find the travel distance x_p that provides the maximum field of view on the retina. The calculated x_p of the designed system is plotted on the left of Fig. 8. Note that the projector position is fixed and that resulting fixed projection region covers an area larger than the HOE size. As shown in Fig. S5, diffraction efficiency decreases from the right edge of the HOE as the HOE moves laterally (gray lines).

Furthermore, some of the light rays leaving the HOE don't make it into the pupil since these rays are not focused to a single point (dotted lines). This is due to the incident angle of the reference beam being different at each point (a diverging reference beam is used), and thus the reconstructed beam having a different diffraction angle at each point. Note that since each ray indicates a different pixel in the virtual retinal display, the observer still can see a clear (albeit incomplete) image even when not all rays converge to a single point. So long as a ray makes it into the pupil it will be observable to the user, just potentially with distortion caused by missing the Maxwellian view point. This image distortion can be solved with predistortion (See Supplementary B.2.2).

Once $x_p(\alpha)$ is calculated, the maximum eye box is derived. The center of Fig. S5 shows a result from the right most border of the eye box. Between the center (x_p = 0) and this right most position, the system always provides >90° horizontal field of view (the FOV at the center). Thus we can calculate the eye box using this simulation. Outside of the eye box, vignetting will cause blind regions and the system can no longer provide a 90° FOV as shown in the right of Fig. S5. Even in this case, the observer can still see a fairly large continuous FOV (in this case, 77.4°). However, the center of this peripheral image gets farther from the fovea as you continue to move the eye. The FOV over gaze angle of the designed system is plotted on the right of Fig. 5.

A.4 Point light source shift vs. HOE shift

As mentioned in Section A.1, due to the finite thickness of the photopolymer, the HOE still maintains some diffraction efficiency for input light under Bragg mismatch conditions. When a Bragg-mismatched light source is incident on the HOE diffraction efficiency is reduced and

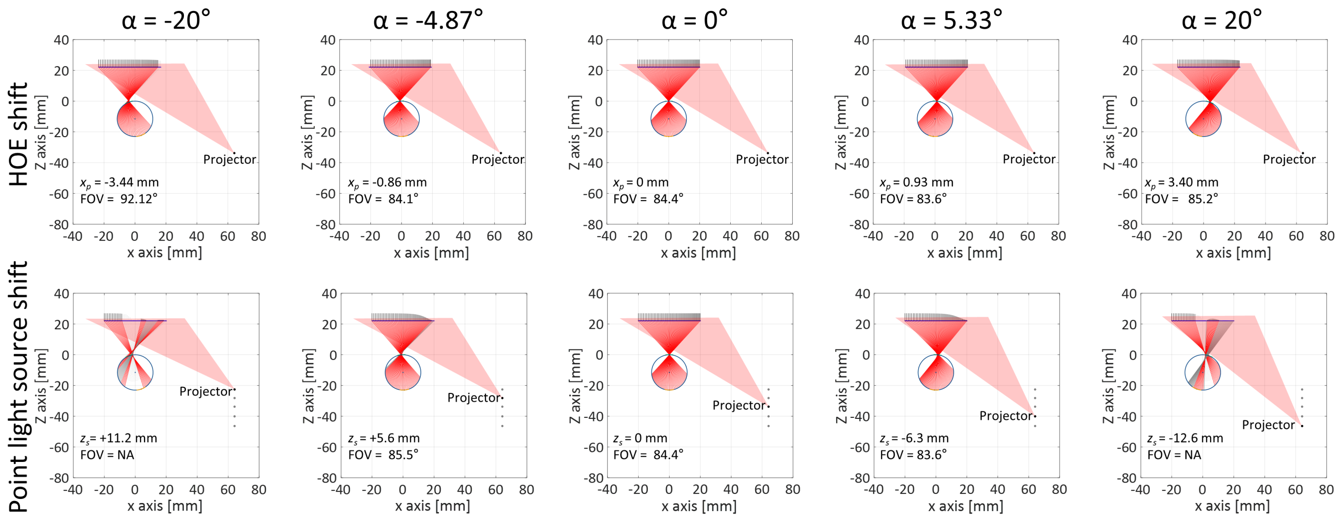

Fig. S6. Eyebox comparison between HOE shifting and point light source shifting. The notation of elements is the same with Fig. S5. Black dots represent the location of the projector and gray dots are used to specify relative position of the projector while shifting. Figures in the same column have the same gaze angle (α). The grey lines indicate low efficiency rays and the dotted lines are the rays cannot go into the pupil. Traveling distances of the HOE and point light source are represented as x_p and z_s, respectively. First row shows the results of the HOE shifting method, which can provide about 40° FOV with 8 mm shifting. However, the moving point light source produces only 10° FOV.

the diffraction angle also changes. As long as sufficient diffraction efficiency is maintained, a single HOE can be used over a wider range of probe beams. In Maxwellian displays using HOEs, this property is used to implement a dynamic eye box by changing the position of the probe beam [Jang et al. 2018, 2017]. It is possible to re-position the eye box using gaze tracking information and the fact that the HOE reproduces the focal point based on the position of the point light source. This method confers the benefits of all optics being fixed and stable (within the HMD), but the eye box is not quite sufficient.

In this work, we propose a method to move the HOE with the position of the point light source fixed in order to implement a dynamic eye box. Fig. S6 compares the resulting eye box, when using the two techniques. The first row provides results for the HOE shift method, while the second row provides results for shifting the point light source. The positions of the two projectors are the same when the gaze angle (α) is 0, i.e., when looking straight forward.

When shifting the point light source, the maximum gaze angle coverage is from -4.37° to +5.33° when the point light source traveled from +5.6 mm to -6.3 mm along z axis. If the projector moves further than this, the FOV of the display will decrease significantly as diffraction efficiency will decrease resulting in a dark portion of the display. However, the laterally shifting HOE from -3.44 mm to +3.40 mm covers the gaze angle from -20° to +20° rotation while preserving its FOV.

In the given situation, the dynamic eye box of the HOE shift method is simulated to 11 mm whereas that of the point light source shift is calculated as 2 mm. The simulation results shows that, under the same experimental conditions, moving the HOE can achieve an eye box that is around five times wider than moving the point light source as shown in the right of Fig. 5 in the manuscript.

A.5 Angular Resolution Analysis with Gaze Angle Changing

A.5.1 Angular resolution analysis of the foveal display .

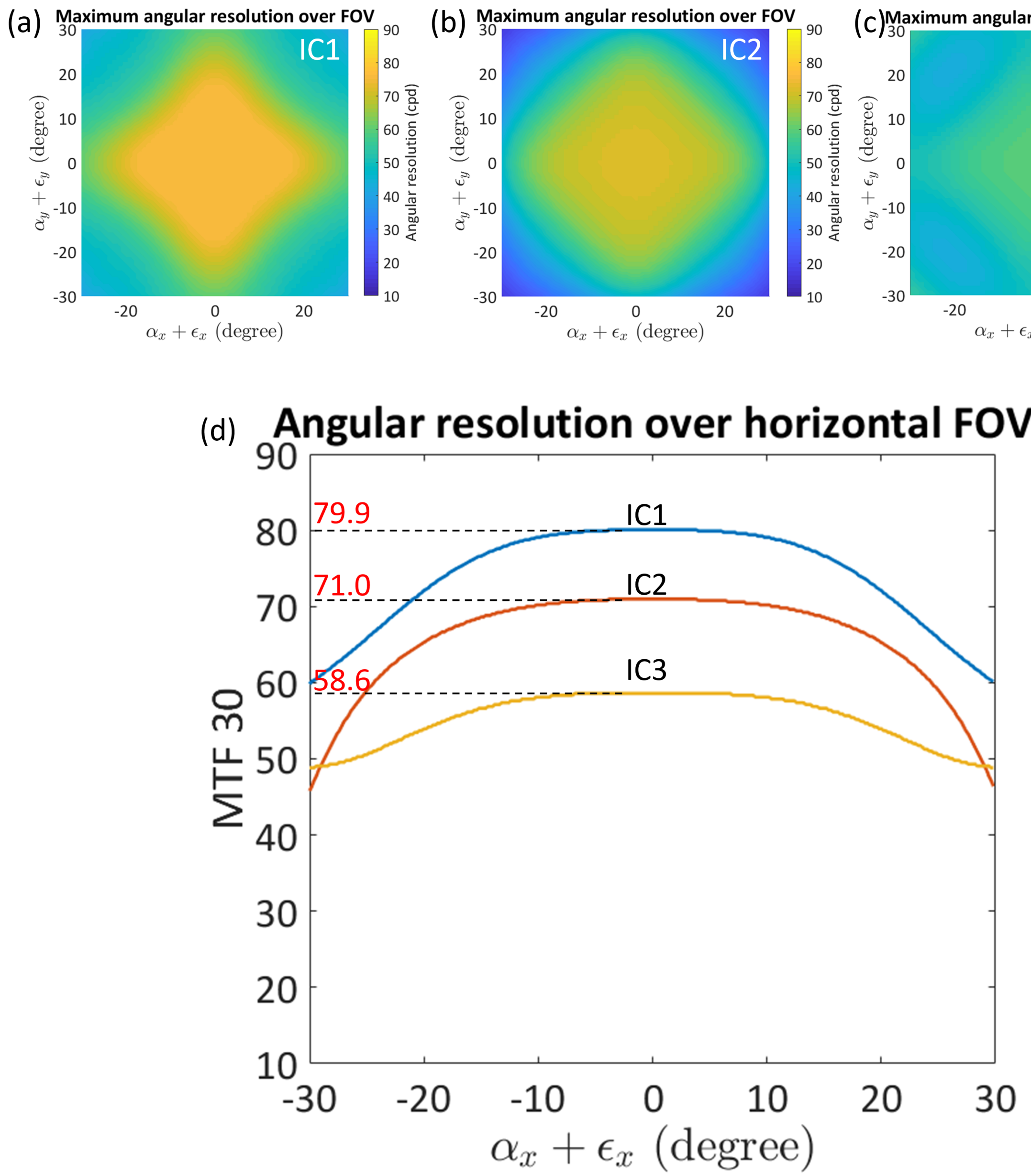

Fig. S7. The optical limitation of angular resolution over FOV in foveal display. Note that both gaze angle ÉŚ and eccentricity Îţ can change the angular resolution. The MTF30 map over the FOV for (a) IC1, (b) IC2, and (c) IC3. (d) The MTF30 graphs of over horizontal FOV. Note that the IC1 has a better optical capability due to the shorter distance between the microdisplay and the image combiner.

Angular resolution limitations of the optical structure. More detailed angular resolution analysis of our foveated AR display over gaze angle and eccentricity is presented in this section. The angular resolution of near-eye display is determined by the pixel density of the display and the optical capability of the image combiner. The angular resolution limitation of the optical structure in the foveal display was calculated by a commercial optic software based on ray tracing.

Figure S7 shows the calculated angular resolution limitations (MTF30) over FOV of the planar ICs used in the prototype. Since the optical structure of the foveal display consists of multiple simple on-axis mirrors, the angular resolution limits were fairly high and symmetric. Ic1, IC2, and IC3 showed sufficient angular resolution capability for ±10° range, which is especially sufficient for foveal region only display (±5°).

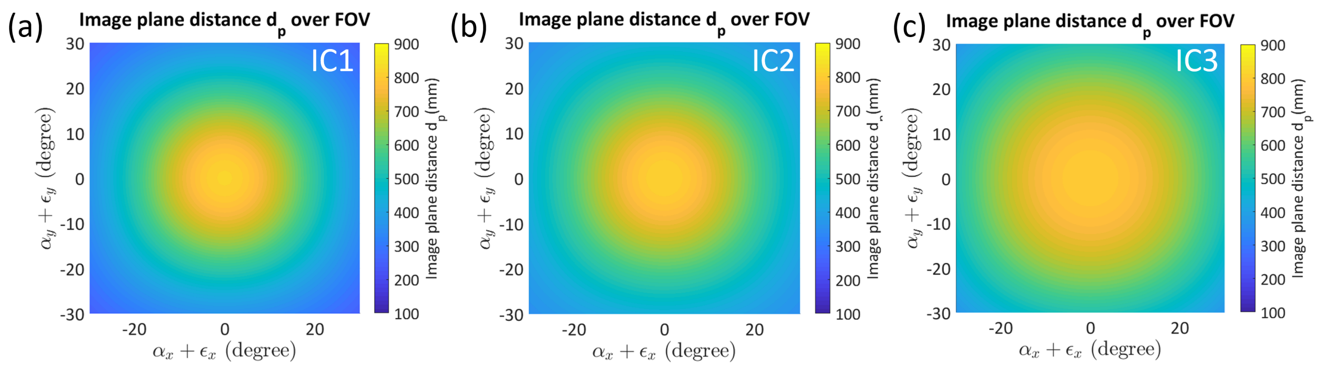

Fig. S8. The image plane distance d_f changes over FOV in foveal display. Note that both gaze angle ÉŚ and eccentricity Îţ affect to the d_f. (a) IC1, (b) IC2, and (c) IC3.

However, when the gaze angle α is far off-axis, the capability rapidly decreases because of the field curvature aberration. In this case, the optical capability might limit the display resolution and causes the resolution decrease.

Due to the field curvature, the image plane distance also changes based on the gaze angle and eccentricity as shown in Fig. S8. However, this focal distance change doesn't decrease the resolution of the foveal display more than in Fig. S7, since only ±5° circle is shown at one time. For example when the observer's gaze angle $\alpha_x, \alpha_y = 10°, 10°$ in the foveal display with IC1, the image plane distance d_f is 658 mm, which is pretty different from the d_f at the center gaze (800 mm). However since only the small region around the fovea is covered by the foveal display, the foveal display will be always within the human eye depth-of-field (0.8D 1D) [Bernal-Molina et al. 2014].

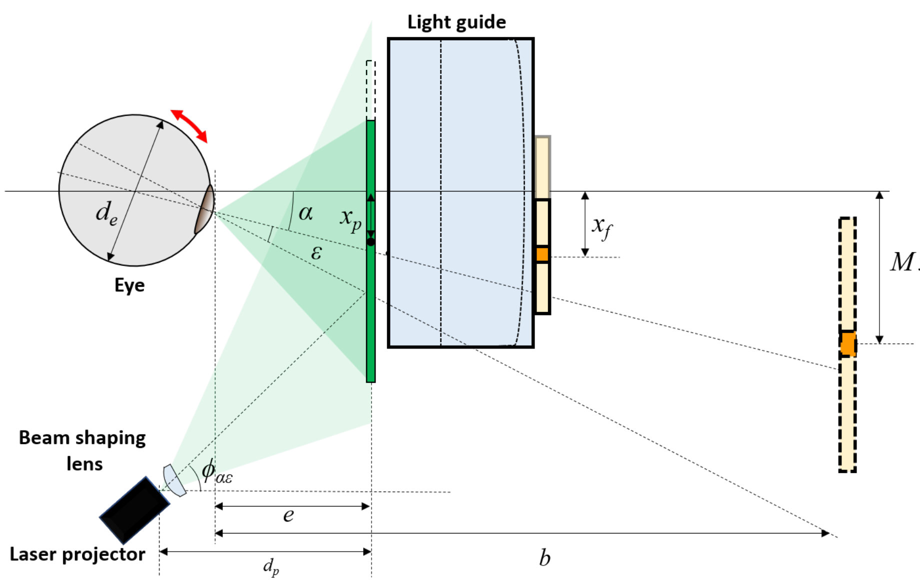

Fig. S9. The schematic diagram of the HOE and micro display movement according to the gaze angle α

Angular resolution of the foveal display . The angular resolution of the foveal and peripheral display are determined using (pixel-based) resolutions for the micro OLED and projector and their geometric relations. Figure S9 shows the simplified schematic diagram of the display when the gaze angle is α. The required travel distance of the micro display x_f is given by

$$x_f = (b + \frac{D_e}{2}) \times \frac{\tan(\alpha)}{M}. \tag{S1}$$

Here, a paraxial approximation is assumed, so the number of pixels of the foveal display ∂N_f per unit length ∂x in the image plane is constant as follows:

$$\frac{\partial N_f}{\partial x}(\alpha, \epsilon) = k_f. \quad (x_{min} \leq x \leq x_{max}) \tag{S2}$$

where $x_{min} = x_f$ - $Mw_d/2$ and $x_{max} = x_f + Mw_d/2$. In order to compute the angular resolution over eccentricity ϵ, the relationship between x and ϵ via α should be considered as follows:

$$x(\alpha, \epsilon) = \frac{d_e}{2}\tan(\alpha) + b\tan(\alpha + \epsilon) \quad \text{and} \tag{S3}$$

$$\frac{\partial x}{\partial \epsilon} = b\sec^2(\alpha + \epsilon). \tag{S4}$$

Now the angular resolution c_f (in cycles per degree) over eccentricity is given by:

$$c_f = \frac{1}{2}\frac{\partial N_f}{\partial \epsilon} = K_f b\sec^2(\alpha + \epsilon). \tag{S5}$$

where K_f is the constant specified by boundary condition:

$$N_{dx} = \int K_f b\sec^2(\alpha + \epsilon)d\epsilon. \tag{S6}$$

Where N_{dx} is the horizontal pixel number of the micro display.

However, this value is not always the actual angular resolution. If the angular resolution of the display pixel is higher than the angular resolution limitations of the optical structure, then the effective angular resolution should be the optical limitation. For example at the large off-axis gaze angle, the angular resolution of the foveal display c_f increases due to the denser pixels in a unit angle, but the optical capability is worse than that because of the field curvature aberration. In this case, the effective angular resolution will be the optical angular resolution limitations as shown in Fig. 8 in the main manuscript.

A.5.2 Angular resolution analysis of the peripheral display .

The angular resolution of the peripheral display c_p can be derived similarly.It is assumed that the number of pixels ∂N_p in a unit projection angle $\partial\phi_{\alpha,\epsilon}$ is constant as follows:

$$\frac{\partial N_p}{\partial \phi_{\alpha,\epsilon}} = k_p. \quad (\phi_{min} \leq \phi \leq \phi_{max}) \tag{S7}$$

where $\phi_{min} = \arctan(\tan(\phi_0) - \frac{w_p}{2d_p})$ and $\phi_{max} = \arctan(\tan(\phi_0) + \frac{w_p}{2d_p})$. The relationship between x in the HOE plane and $\phi_{\alpha,\epsilon}$ is given by:

$$d_p\tan(\phi_{\alpha,\epsilon}) = d_p\tan(\phi_0) - x(\alpha, \epsilon) \quad \text{and} \tag{S8}$$

$$\frac{\partial \phi_{\alpha,\epsilon}}{\partial x} = -\frac{1}{d_p\sec^2\phi_{\alpha,\epsilon}}. \tag{S9}$$

The relationship between x in the HOE plane and eccentricity ϵ is given by:

$$x(\alpha, \epsilon) = \frac{d_e}{2}\tan(\alpha) + e\tan(\alpha + \epsilon) \quad \text{and} \tag{S10}$$

$$\frac{\partial x}{\partial \epsilon} = e\sec^2(\alpha + \epsilon). \tag{S11}$$

By combining Eqs. (S7), (S9), and (S11), angular resolution c_p (cycles per degree) over eccentricity is given by:

$$c_p = \frac{1}{2}\frac{\partial N_p}{\partial \epsilon} = \frac{K_p e\sec^2(\alpha + \epsilon)}{d_p\sec^2(\phi_{\alpha,\epsilon})}. \tag{S12}$$

where K_p is the constant specified by boundary condition:

$$N_{px} = \int \frac{K_p e\sec^2(\alpha + \epsilon)}{d_p\sec^2(\phi_{\alpha,\epsilon})}d\epsilon. \tag{S13}$$

Where N_{px} is the horizontal resolution of the projector. Note that c_p has the minimum value when $\alpha, \epsilon = 0$.

B IMPLEMENTATIONS

B.1 Holographic Optical Element Recording

B.1.1 Full-color Holographic Optical Element Recording Setup.

Holographic Optical Elements (HOEs) are created by exposing a holographic recording medium to overlapping, mutually coherent *probe* and *signal* laser beams. Typically, the goal of a holographic recording setup is the reproduction of signal and probe beams, representative of those present when the HOE is in use in its final (exposed) state, at the location of the holographic recording medium. The exceptions to this idea are, generally, limited to exploiting the symmetries inherent in the physics of hologram recording. See, for example, the section on phase conjugated recording (Section B.1.2). The bulk of a holographic recording setup (away from the location of the holographic recording medium) is simply used for preparing suitable, mutually coherent, laser beams for the final set of optics which shape the signal and probe beams. In figure S10 the holographic recording medium (along with its substrate) is shown schematically in the lower right hand corner as a light blue rectangle. The object and reference beams are the outline of triangles which intersect the holographic recording medium. One may think of the rest of the holographic recording setup in two stages – the "white light" laser source and the shaping of the signal and probe beams.

White light laser source. The requirements for the white light laser source are that the light must be sufficiently intense, there must be an appropriate balance of power between the red, green, and blue light, and the light from the signal and probe beams must have a stable phase relationship. The phase relationship is insured by making sure that the difference in the path length from the laser source to the holographic recording medium through either the probe beam or the signal beam path is less than the coherence length of each color laser. The coherence length of each of our lasers is greater than 15 meters which is much larger than any difference in path length in the setup. In figure S10, the white light laser source is the region of the figure where the paths of the light are illustrated in color. The individual lasers which go into building the white light laser are shown schematically in figure S10 on the left hand side of the figure. The red laser is a 500 mW Cobolt Flamenco operating at 660 nm. The green laser is a 1 W Cobolt Samba operating at 532 nm. The blue laser is a 500 mW Coherent Genesis MX operating at 460 nm. When operated at their maximum operating power, all three lasers emit nearly perfectly Gaussian beams and no other filtering of the beams is necessary. In all of our experiments, therefore, all three lasers were operated at their maximum operating power and intensity control was handled in other parts of the beam path. Immediately after each of the lasers, two front surface mirrors (ThorLabs P/N: PF10-03-P01) were used to direct the laser beams into the experiment. Following the mirrors a set of diverging and converging lenses (focal lengths -25 mm and 100 mm, spaced by 75 mm, ThorLabs P/Ns: ACN127-025-A and AC254-100-A-ML) expand the diameters of the laser beams by 4× their original size. During alignment of these lenses (and all other beam expansion optics), the beam quality was checked with a shearing interferometer (ThorLabs P/N: SI254) to insure that the beams remained plane waves. Following the beam expansion, each color laser beam propagates to the optics which are used to balance the power between the individual single color beams. This is accomplished with a half wave plate appropriate for each wavelength (ThorLabs P/Ns: WPH05M-473, WPH05M-532, WPH05M-670), a polarizing beam splitter (ThorLabs P/N: PBS121), and a beam block (Thorlabs P/N: LB1). Depending on the orientation of the half wave plate, the polarization of each laser beam is rotated from the nominally vertical polarization of each laser. The horizontally polarized component of the light proceeds through the polarizing beam splitter while the vertically polarized component is deflected to the side. The vertically polarized light from the red laser proceeds directly to dichroic mirrors (ThorLabs P/Ns: DMLP490, DMLP567) where it is combined with the green and blue laser beams. The blue and green laser beams are directed by a silver front surface mirror towards the dichroic mirrors. All the optics in the holography set up are maintained in the same horizontal plane to maintain the polarization in all parts of the path where the beam is not being altered. At this point, the three laser beams have been combined into one "white light" laser beam. A electronically controlled shutter (ThorLabs P/N: SH1/M) determines whether or not the beam propagates to the rest of the optics in the experiment and the timing of exposures.

Creation and shaping of the probe and signal beams. After the shutter, front surface mirrors direct the beam to the rest of the setup. In the figure, those mirrors are denoted as being on flip mounts (ThorLabs P/N: FM90/M) which allows the light from the lasers to be used in different experiments. At this point the white light laser beam is split into the probe and signal beams. We are able to change the relative power ratios of the two beams by using a similar setup of half wave plate and polarizing beam splitter. This time, to maintain the relative balance of powers in each wavelength we use a superachromatic half wave plate (Thorlabs P/N: SAHWP05M-700). In figure S10, the probe beam is the upper beam path beam which is deflected by 90° at the polarizing beam splitter. The signal beam travels, undeflected, towards a front surface mirror. After this polarizing beam splitter, the reference and probe beams have different polarization. To create an interference pattern between the two beams, the polarization of both beams must be the same; so, the polarization of one of the beams must be rotated. This is accomplished with yet another combination of superachromatic half wave plate and polarizing beam splitter. In the figure the polarization of the vertically polarized probe beam is rotated to horizontal. In our experiments some holograms were created with both beams horizontally polarized while other holographic optical elements were created with vertically polarized beams. In figure S10, vertical polarization could be achieved by removing the last set of half wave plate and polarizing beam splitter from the probe beam and placing them in the position of the last mirror which redirects the signal beam. Both beams must be expanded to fill the input apertures of the final lenses which will do the final stage of beam shaping. The probe beam undergoes two stages of expansion. The first stage of expansion expands the beam by 7.5× using a pair of achromatic lenses with focal lengths −20 mm and 150 mm spaced by 130 mm (Thorlabs P/Ns: ACN127-020-A and AC254-150-A). The second stage further expands the probe beam by 2× using a lenses with focal lengths of -50 mm and 100 mm (ThorLabs P/N: ACN254-050-A,

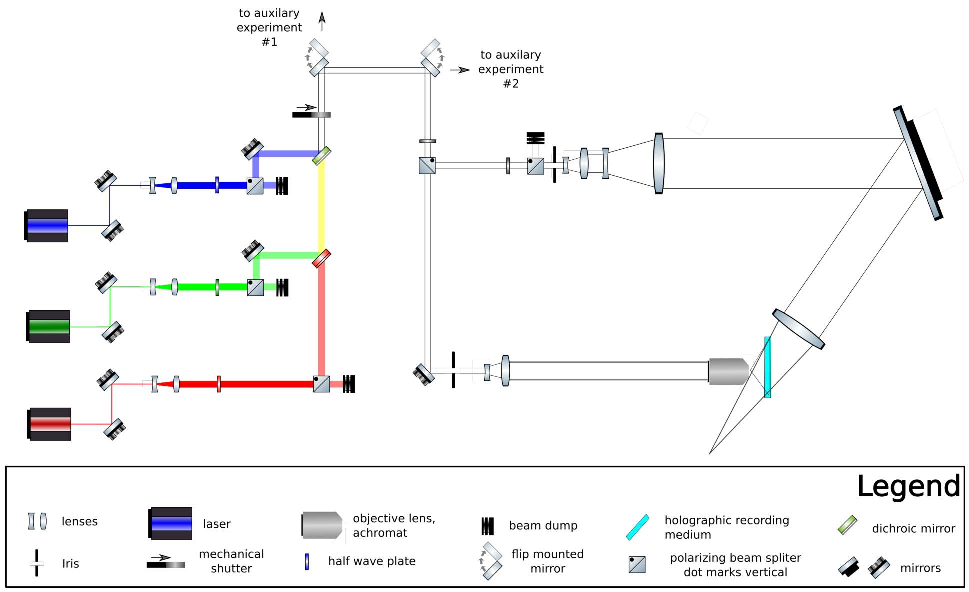

Fig. S10. Full-color HOE recording scheme

Edmund Optics P/N: 33-921) spaced by 50 mm. The probe beam, then, propagates to a three inch diameter front surface mirror (ThorLabs P/N PF30-03-P01) which directs the beam towards an achromatic lens (Edmond Optics P/N: 33-922) which focuses the beam in the region of the holographic recording medium. This lens was chosen to create a cone of light similar to the projection cone of the scanning laser projector and to cover the width of the intended HOE. The signal beam undergoes one stage of beam expansion using a pair of achromatic lenses with focal lengths -50 mm and 300 mm spaced by 250 mm. From the beam expanding optics, the beam propagates to an achromatic objective lens with an effective focal length of 3 mm (Olympus UPLFLN 60X). After quickly coming to a focus, the signal beam diverges to fill the location of the holographic recording medium. The holographic recording medium and its glass substrate were held in place with a 3D printed mount made especially for that purpose. The glass substrates were cut to approximately 3 inch × 2 inch rectangles. The holographic recording medium was Covestro's Bayfol HX films which were applied to the glass substrates. Holographic optical elements were made for both single color (green) operation and three color (red, green, and blue) operation. During exposure of single color holographic elements, there was no need to balance the power densities in each of the beams – the the red and blue lasers were simply turned off. For full color (RGB) HOEs the power density of each color was adjusted to be inversely proportional to the absorption of the holographic film at each wavelength. For wavelengths in our lab, this works out to be approximately in the ratio of 3:7:14 (red:green:blue). Exposure times ranged from tens of seconds to low hundreds of seconds; but, tended to be approximately one minute. Because vibrations of the optical setup would blur out the interference pattern which is necessary for creating the hologram, all exposures were done on an optical table with active isolation legs (Thorlabs P/Ns T1225P and TF1225A7).

B.1.2 Phase-Conjugated Recording Method.

The most common way of creating holographic optical elements is to use the same signal and probe beams which are intended to be used in the operation of the holographic optical element in the creation of the holographic optical element. This choice simplifies design decisions at the outset. Occasionally, though, this direct path leads to the requirement to use traditional optical elements in the holographic recording set up which are difficult or impossible to obtain. The signal beam for the holographic optical element in this study, for instance, comes to a focus approximately 22 mm away from the holographic optical element and the rays from the signal beam have a spread of directions of about 85 degrees. Even if the recording setup allowed the last lens in the shaping of the signal beam to abut the holographic film, this final lens would have to have an exit aperture with a greater than 40 mm diameter, an f-number of 0.55 or less and would have to be chromatically corrected to have the same focal length for the three wavelengths used to create the hologram. Lenses with this set of requirements are *difficult* to find. For example, objective lenses which have been highly color corrected exist with appropriate f-numbers exist; but those lenses have small input and output apertures of approximately 1 cm and 1 mm. The solution to this quandary is to use the fact that the physics which is used to create the holographic optical element obeys time reversal symmetry. That is, if a holographic optical element is created which converts a given probe beam into a given reconstructed signal beam, the holographic optical element will create the “time-reversed” signal beam from the “time-reversed” probe beam.

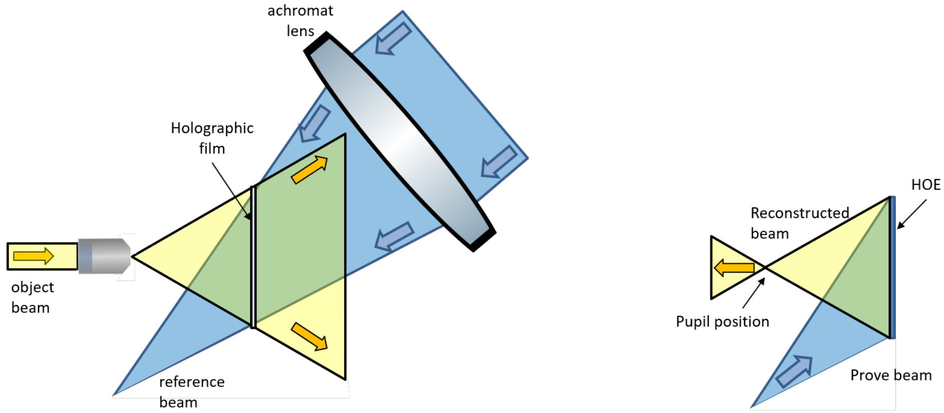

Fig. S11. Phase conjugate recording and reconstruction of HOE (a) Recording and (b) Reconstruction

Figure S11 consists of two sketches. The sketch on the left (part a) shows how the holographic optical elements used in our study were recorded. The sketch on the right (part b) shows how they are used in our prototypes. The large, yellow or blue, geometrical shapes (rectangles, triangles, trapezoids) show the shapes of the probe and signal (object) beams. The colored arrows show the direction of propagation of the beams. Note that, in both sketches, the shape of the beams just to the left of the holographic optical element (in part b) or the holographic film (in part a) are the same. Note also, that the difference between a light beam and the time-reversed light beam is only in the direction of propagation. That is, if you represented the propagation of a beam of light by a super-slow motion movie of a pulse of light propagating through space, the time reversed beam of light would be represented the same movie run backwards – the pulse would be the same shape; but moving in the opposite direction. Since the physics holography respects time reversal symmetry, a holographic optical element created with the set of beams illustrated in part a of figure S11 can be used in the configuration shown in part b.

This trick of exploiting time reversal symmetry in holography is called *phase conjugate recording* or *phase conjugate illumination*. The lack of reference to time reversal symmetry in the nomenclature comes from a historical technicality: when writing the expression of the electric fields associated with the light beams, the time-reversed beam corresponds to writing down the complex conjugate of the spatial part of the beam; so, the “time-reversed” beam is frequently referred to as the “conjugate beam.” The end result is that this conjugate recording method allows one to use an objective lens which has the necessary f-number and chromatic aberration correction which is readily available off-the-shelf as opposed to a much larger diameter custom made lens which is not readily available commercially.

B.1.3 Stacking Multiple HOEs.

To implement a full-color peripheral display, an HOE that operates independently on at least three wavelengths is required. In this study, three independent HOEs are recorded and vertically stacked. Thanks to the thinness of the photopolymer, this method has the advantage of maximizing the efficiency of each HOE color without significantly affecting the form factor of the system. If three wavelengths are recorded on a single photopolymer, the diffraction efficiency is degraded and the uniformity of the color may be reduced. To avoid misalignment problems that may occur during the stacking process, each HOE is stacked sequentially, alternating between recording and attaching process, rather than being stacked after recording as shown in Fig. S12. With a fixed HOE mount on the recording setup, it can be assured that the hologram is always recorded in the same position of the HOE. After stacking three HOEs vertically, the full-color HOE is sealed and prepared to be used on the setup. Figure S13 shows the stacked HOEs for full-color display, its thickness measurement. The HOE is cut into the shape and mounted to a holder and linear stages. Note that the thickness of the HOE includes thickness of films for sealing. We utilized both a stacked HOE (full-color results) and a film HOE (monochrome results, wearable prototype and some of the full-color results) in this study.

B.2 Calibrations

B.2.1 Geometric Calibration.

In foveated displays, the geometric relationship between the foveal and peripheral displays changes constantly based on the fovea position and the gaze angle. Therefore, it is necessary to calculate image transformations for all possible cases. We captured a checker board pattern

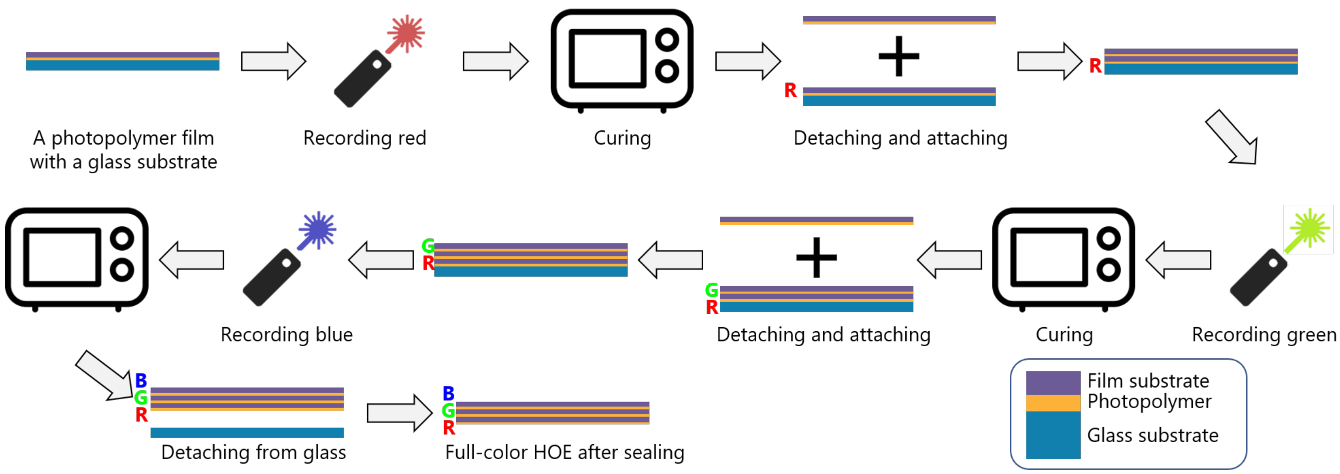

Fig. S12. Stacking three layers of HOE method for the better uniformity and higher diffraction efficiency

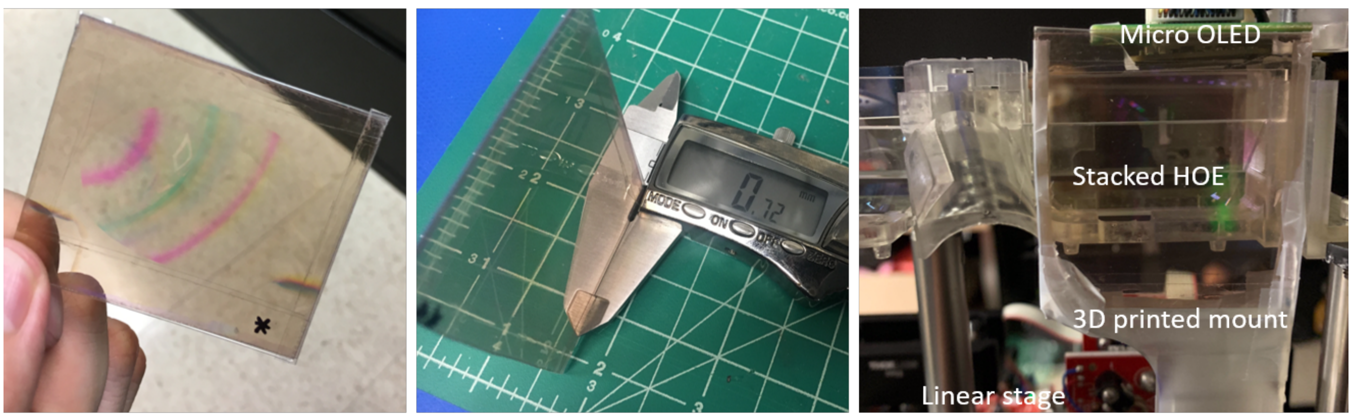

Fig. S13. Prepared stacked HOE for full-color images (left) Full-color stacked HOE after sealing (center) the total thickness of the HOE is 0.72 mm (right) HOE cut into the shape and mounted to a holder. This holder was connected to the 2-dimensional linear stages.

with the Pixel 2 camera for each micro OLED position and HOE position over the entire FOV and ±20° gaze angle coverage. Then, the transformation functions were calculated from the extracted grid points for each case. Second order polynomial functions were used for the fit instead of homography because the diffraction reaction at the HOE gratings was non-linear. After, the ±5° foveal region and peripheral region were set at the target image and each of them was transformed to the micro OLED and laser scanning projector base image.

Figure S14 shows the entire process of the calibration and the base image generation method with the checkerboard patterns. First, the checkerboard images for the foveal and peripheral displays were generated. Second, the checkerboard images were captured at the all possible positions within the FOV and the gaze angle coverage. Please note that at the given gaze angle, the checkerboard image for the peripheral display was captured once while the checkerboard images for the foveal display were captured 8 times with the different micro OLED position to cover the entire FOV. Then, the coordinates of the grid points were extracted from the captured checkerboard images. Then we calculated the transformation equations of the grid points between the captured checkerboard image and the input image in the peripheral display G_p, the captured checkerboard image and the input image in the foveal display G_f and the captured checkerboard images at the center gaze and the gaze angle α H_f. The transformations were fitted with the second order polynomial equation instead of the homography, to precisely compensate the non-linear image transformation at the HOE gratings.

After, the base images for foveal and peripheral images can be calculated. Since the virtual 3D images should be remained at the virtual spaces regardless of the observer's gaze angle, the target image was first calculated at the center gaze as shown in the bottom-left of Fig. S14. Then, the target image at the given gaze angle was calculated with H_f. Finally, the base images for the micro OLED display and for the laser

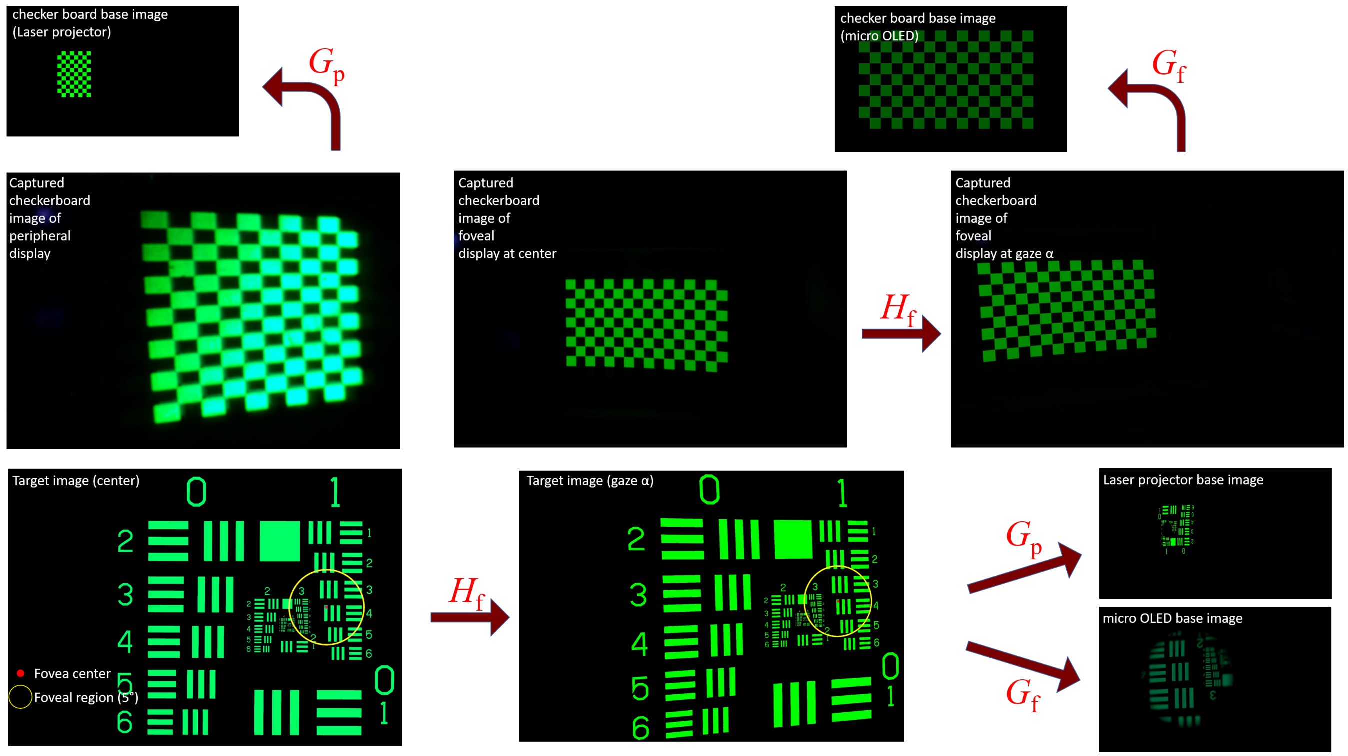

Fig. S14. The geometric calibration of foveal and peripheral display and the base image generation method for a certain gaze and a fovea position (top) input checkerboard images for peripheral and foveal displays (middle) captured checkerboard images at the center gaze and the gaze angle α (bottom) Target images at the center gaze and gaze angle α and the generated base images for the micro OLED and the laser scanning projector

scanning projector were generated based on G_p and G_f as shown in the bottom-right of Fig. S14.

B.2.2 Multiple Display Color Calibration.

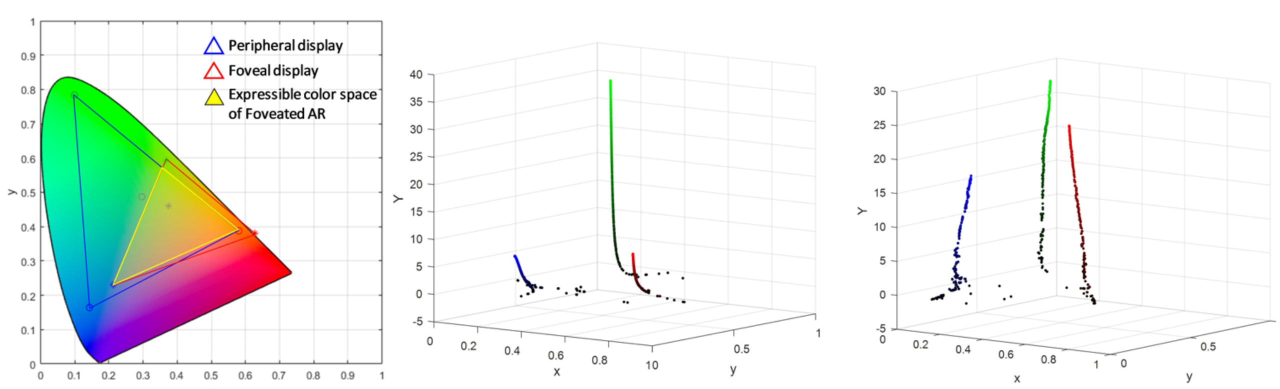

Fig. S15. The color and intensity calibration of foveal and peripheral display (left) color space of foveal (red), peripheral (blue) and overlapped region for Foveated AR display (yellow). (center) measured color gamut of the foveal display in CIE xyY space. (right) measured color gamut of the peripheral display in CIE xyY space.

Since a color filter-based micro OLED display and a laser diode-based scanning projector were used for the foveal and peripheral display respectively, the color and intensity of both displays required appropriate matching. The wavelength/angular selectivity of the HOE further modifies the color/intensity of the laser projector before arriving at the user's pupil. We measured the intensity and color value of each channel of the foveal and peripheral display at the pupil position with a spectroradiometer (Gamma-Sci, GS-1160, customized for AR display). Theoretically, both displays can provide all colors inside the overlapped triangle in color space with reduced bit depth by using the correct color conversion matrix and a precise look up table (See supplementary B.2.2). However, in practice, a fine-tuning at the final stage was required due to the color shift of the laser diode across operating temperature and the maximum current limitation mechanism of the micro OLED driving board.

The laser scanning projector and the micro OLED have different color primaries and different display gamma. Furthermore, the reflective surfaces and diffraction in HOE medium might cause color and intensity shift of the foveal and peripheral display. Therefore, the color and intensity calibration of the foveal and peripheral display should be accomplished for the natural fusing. Especially in the peripheral display, the laser scanning projector has 5 different color primaries itself and their spectral reaction to the each HOE layer are all different. So precise calibration of two displays should be done by intensity and color measurement.

A spectroradiometer from Gamma-Sci (GS-1160) was used in the measurement experiment. The relative luminance (Y) and the color value (x,y) of reference images (256 images for each color) were measured (10 times per image) in descending order. The displays were stabilized for 30 minutes before the experiment. As shown in Fig. S15, the 3 color primaries for foveal display ($x_{F,R}$, $x_{F,G}$, $x_{F,B}$, $y_{F,R}$, $y_{F,G}$, $y_{F,B}$) and peripheral display ($x_{P,R}$, $x_{P,G}$, $x_{P,B}$, $y_{P,R}$, $y_{P,G}$, $y_{P,B}$) and the gamma function of each channel for foveal display ($Y_{F,R}(R)$, $Y_{F,G}(G)$, $Y_{F,B}(B)$) and peripheral display ($Y_{P,R}(R)$, $Y_{P,G}(G)$, $Y_{P,B}(B)$) are obtained, where R, G and B are the pixel value of the input image. From the measurement, lookup tables for each color channel and for each display has been obtained.

The prototype can provide the colors in the overlapped region in the color space (yellow triangle in Fig. S15). We can compute the new color primaries with the simple geometric relation. ($x_{Disp,R}$, $x_{Disp,G}$, $x_{Disp,B}$, $y_{Disp,R}$, $y_{Disp,G}$, $y_{Disp,B}$). With these new color primaries, we can set a gamma value γ_{new} of our display and a proper white balance properly. So when the target image's pixel value is (R_{target}, G_{target}, B_{target}), the target luminance ($Y_{target,R}$, $Y_{target,G}$, $Y_{target,B}$) is calculated as follows:

$$Y_{target,R} = \kappa_R \times R_{target}^{\gamma_{new}} \quad Y_{target,G} = \kappa_G \times G_{target}^{\gamma_{new}} \quad Y_{target,B} = \kappa_B \times B_{target}^{\gamma_{new}} \tag{S14}$$

where κ_R, κ_G and κ_B are the white balance coefficient for each color channel, respectively. From the linearity of CIE XYZ and the definition of CIE xyY, the target color value x_{target}, y_{target} and Y_{target} are as follows:

$$x_{target} = \frac{(x_{Disp,R}/y_{Disp,R})Y_{target,R} + (x_{Disp,G}/y_{Disp,G})Y_{target,G} + (x_{Disp,B}/y_{Disp,B})Y_{target,B}}{Y_{target,R}/y_{Disp,R} + Y_{target,G}/y_{Disp,G} + Y_{target,G}/y_{Disp,G}}, \tag{S15}$$

$$y_{target} = \frac{Y_{target,R} + Y_{target,G} + Y_{target,B}}{Y_{target,R}/y_{Disp,R} + Y_{target,G}/y_{Disp,G} + Y_{target,G}/y_{Disp,G}} \quad \text{and} \tag{S16}$$

$$Y_{target} = Y_{target,R} + Y_{target,G} + Y_{target,B}. \tag{S17}$$

The foveal and peripheral display should reproduce this color by mixing their primaries. The mixing equation is similar to Eqs. (S15)-(S17). The required luminance of foveal display for the target ($Y_{F,R}$, $Y_{F,G}$, $Y_{F,B}$) can be calculated from the matrix inversion.

$$\begin{pmatrix} \frac{x_{target}-x_{F,R}}{y_{F,R}} & \frac{x_{target}-x_{F,G}}{y_{F,G}} & \frac{x_{target}-x_{F,B}}{y_{F,B}} \\ \frac{y_{target}-y_{F,R}}{y_{F,R}} & \frac{y_{target}-y_{F,G}}{y_{F,G}} & \frac{y_{target}-y_{F,B}}{y_{F,B}} \\ 1 & 1 & 1 \end{pmatrix} \begin{pmatrix} Y_{F,R} \\ Y_{F,G} \\ Y_{F,B} \end{pmatrix} = \begin{pmatrix} 0 \\ 0 \\ Y_{target} \end{pmatrix} \tag{S18}$$

With the lookup tables obtained from the measurement, the required pixel value of the foveal display (R_f, G_f, B_f) can be calculated. The required pixel value of the peripheral display (R_p, G_p, B_p) can also be calculated similarly.

Even with these principles, the prototypes required a fine-tuning process at the final stage, because of the wavelength shift of the laser diode due to the temperature change and the maximum current limitation of the micro OLED driving board. Figure S16 shows the color calibration results of the optical bench prototype. Even with the correct geometric calibration, the fovea and the periphery border was vivid because of the color difference. With the correctly matched color, the foveal and peripheral display were well blended together. The bottom examples of Fig. S16 show that the colors were well-matched for all red, green and blue channels and for the white image.

B.2.3 Blending algorithm for fovea-periphery transition region.

The visual system is specialized in detecting misalignment[Levi et al. 1985] and discontinuities[Kulikowski and King-Smith 1973], and the sensitivity is especially strong when it occurs across a large area in the visual field. To avoid a frequency shift at the exact boundary of the foveal display and compensate for any lingering miscalibration, we applied a linear blending algorithm to the transition region between foveal and peripheral views. A Gaussian blur was applied to the foveal target image from 3-5° eccentricity as the blur kernel was linearly

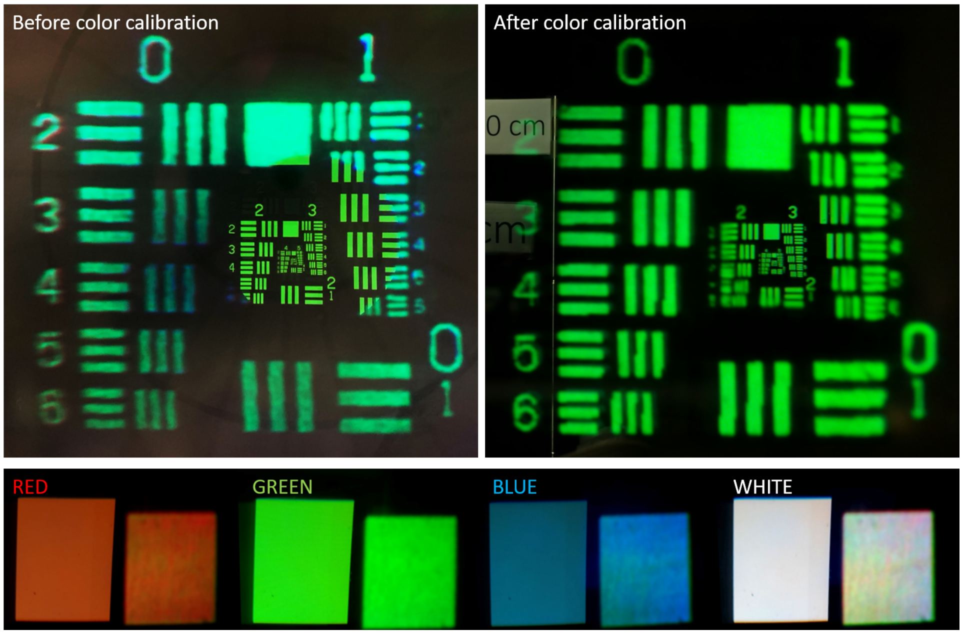

Fig. S16. The color calibration results in the Optical bench prototype (top) the comparison between without and with the color calibration (bottom) the calibrated results for each color channel (left - foveal display, right - peripheral display)

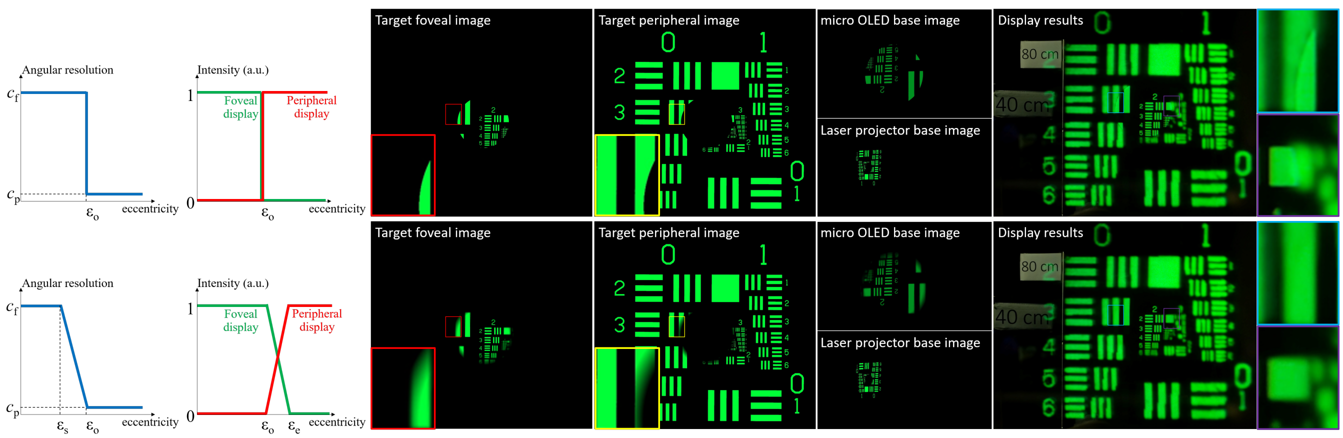

Fig. S17. The blending algorithm for the transition region between foveal and peripheral display (top) without the blending algorithm (bottom) with the blending algorithm

increased in size to match the peripheral resolution. Further, intensity blending was applied to both the foveal and peripheral target images from 5-6° eccentricity for smoother transition.

The smooth transition between the foveal and peripheral display is very important for the natural perception. Figure S17 shows the example of the foveal and peripheral image generation without and with the blending algorithm. Without the blending algorithm, the resolution was discontinuously shifted from foveal display resolution c_f to peripheral display resolution c_p at the fovea border ϵ_o. The foveal display intensity was also changed at the border from maximum to zero (and zero to maximum for peripheral display). These discontinuity creates a noticeable circular line of border in the display results.

In the blending algorithm, the Gaussian blur was applied to the transition region of foveal display for the continuous angular resolution change. As shown in the bottom-left of Fig. S17, the Gaussian blur size is gradually increased from ϵ_s to ϵ_o, so the image of the foveal display border is as blurred as the peripheral display. Further, the intensity of the foveal and peripheral display was linearly mixed from ϵ_o to ϵ_e eccentricity. This additional intensity blending provided the more natural blending of two displays and the additional stability for the geometric calibration. In the right of Fig. S17 shows the display results with and without the blending algorithm. Without the blending algorithm (top) the transition border was observed due to the defocus blur change. Whereas the transition is much more smooth/natural with the blending algorithm (bottom).

C DISPLAY ASSESSMENT EXPERIMENTAL RESULTS

C.1 Gaze coverage experiment

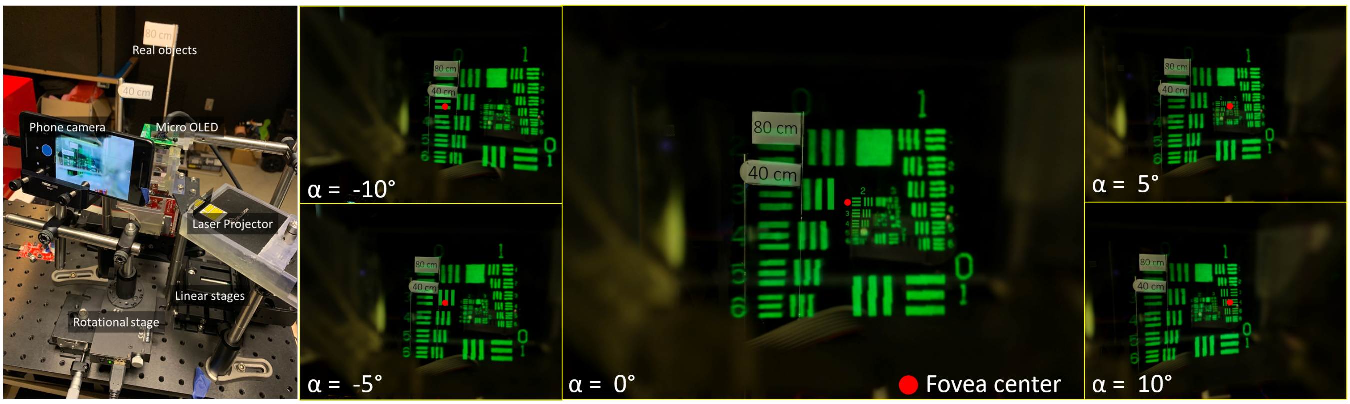

Fig. S18. Gaze angle coverage results for optical bench prototype with IC2. (left) The experimental setup for gaze angle coverage. Note the the center of rotation is 12 mm apart from the camera aperture plane. (right) The captured results for gaze angle coverage experiment. Note that the fovea center is always located at the same position over the gaze coverage.

Figure 15 in the main manuscript showed that the optical bench prototype covers ±20 gaze angle. In this chapter, the detailed experimental results are presented. In the left of the S18 shows the experimental setup for the gaze angle coverage. The Pixel 2 camera was mounted on the rotational stage, and captured the display with a 1-degree angular interval from -20 degree to +20 degree (See supplementary video). Note that the lens entrance pupil is 12 mm apart from the rotation center, to mimic the human eye rotation. The micro OLED display and the HOE were moving according to the gaze angle, and the base images for the both foveal and peripheral display were generated based on the method introduced in Section B.2. In the right of Fig. S18, some of the captured images are shown. The virtual resolution chart image is located at the 80 cm, at the center direction. The red dots indicate the fovea center and they are located at the same position over the gaze angle.

C.2 FOV and Eye box measurement

The FOV of foveal and peripheral display was measured for display assessment. The FOV of foveal display was measured directly with a real FOV target as shown in Fig. S19. The real FOV target and the foveal display were augmented and the instant FOV was measured for all fabricated ICs. The measured horizontal FOV of the foveal display with IC1, IC2 and IC3 was ±15, ±11 and ±7, respectively, and all of them were a little bit smaller than the expected value (±16, ±12 and ±8 respectively). It was because the distance between the camera and the IC was a few mm longer than as designed because of the HOE thickness and the 3D printed holders. The measured vertical FOV of the foveal display with IC1, IC2 and IC3 was ±8, ±6 and ±3, respectively, and all of them were a little bit smaller than the expected value too (±10, ±7 and ±5 respectively).

The FOV of peripheral display wasn't able to be measured with this direct method. As shown in the right of Fig. S19, the horizontal and vertical FOV were larger than the maximum FOV of the camera (Pixel 2). Therefore we captured a top and side view of the peripheral display with a 1 mm grid paper and the footprint of the diffracted light showed the FOV of the peripheral display. Figure 12 in the main manuscript and Fig. S20 shows the measured horizontal and vertical FOV of the peripheral display. The optical bench prototype provided 85 degrees in horizontal and 78 degrees in vertical (101 degrees diagonal) at the center. The eye relief was 22 mm.

Similarly, the eye box of the peripheral display was measured indirectly. The HOE shift in horizontal and vertical direction generated the dynamic eye box, and the pupil shift and the FOV were simultaneously measured from the top view and the side view image. In the bottom of Fig. 12 in the main manuscript and in the right of Fig. S20 shows the measured dynamic eye box of peripheral display in the horizontal and vertical direction, respectively. The optical bench prototype provided 12 mm × 8 mm dynamic eye box, while preserving its FOV. The horizontal and vertical FOV in the dynamic eyebox were 81 ~ 87 degrees and 74 ~ 78 degrees, respectively.

The eye box of the foveal display was directly measured. Since the foveal display is a simple on-axis magnifier system, the eye box was static and bigger than that of the peripheral display. The ±5-degree foveal region was observed within 47 mm × 15 mm static eye box in the

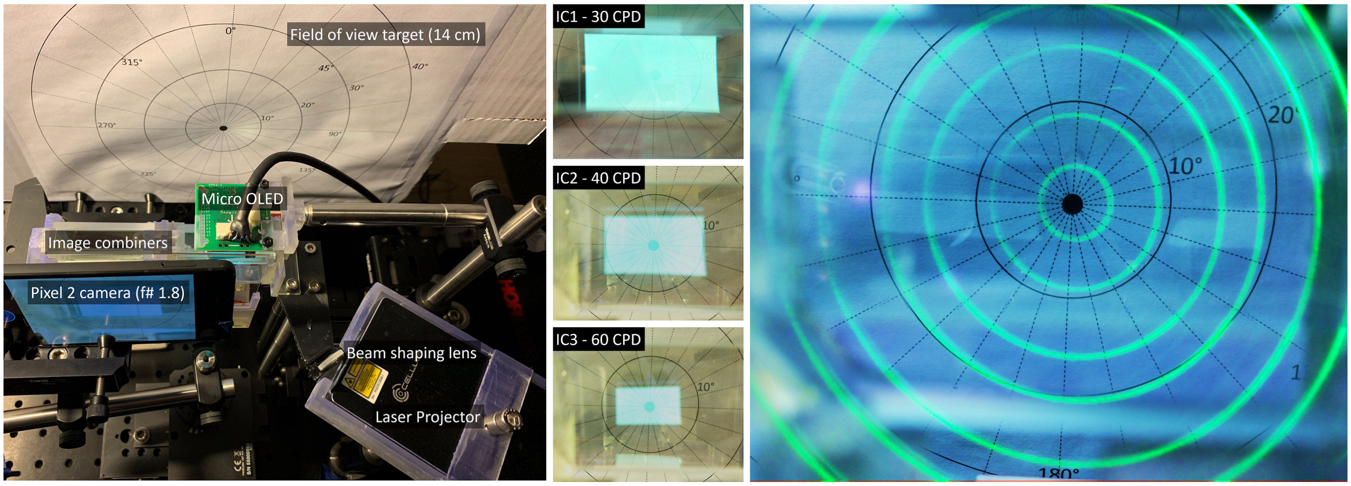

Fig. S19. Direct FOV measurement experiment for foveal and peripheral display with the FOV target (left) experimental setup. The FOV target is located at 14 cm from the camera. (center) Measured FOV of the foveal display with three different image combiners (IC1, IC2 and IC3) (right) The direct FOV measurement for peripheral display. Note that the FOV of peripheral display is larger than the FOV of Pixel 2 camera (F-number 1.8).

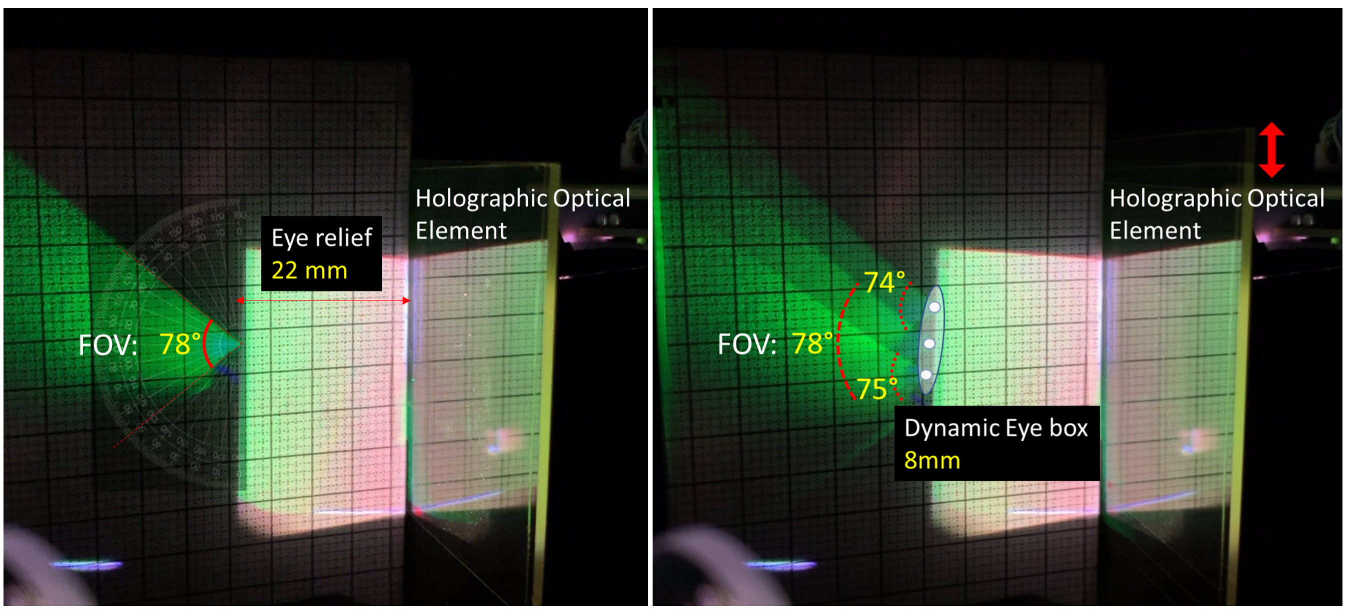

Fig. S20. Indirect FOV measurement experiment and eye box measurement experiment for peripheral display in the vertical direction (left) Measured vertical FOV of the peripheral display. (right) The dynamic eye box results in the vertical direction. Note that the vertical FOV is preserved in the 8 mm dynamic eye box

foveal display with IC2 as shown in Fig. S21. It was actually larger than the calculated value in Section 3.1, because the Eq. (5) was for the whole micro display panel, not the 5-degree foveal region. The eye box of the foveal display with IC1 and IC3 were similarly sufficient.

C.3 Focus changing experiment

The optical bench prototype provides focal cue over the diopters. As shown in Fig. 2 in the main manuscript, the micro OLED display is imaged to the virtual plane with a simple magnifier. By vertically moving the micro OLED display panel, the optical path length from the panel to the magnifier is changed, so that the focal plane is shifted. However, the peripheral display is all-in-focus so the angular resolution and the blur size shouldn't change when the camera focus changes.

Fig. S21. Eye box measurement experiment for foveal display with IC2. Center view images and right-most, left-most, top-most, bottom-most images are shown. Measured eyebox was 47 mm in horizontal and 15 mm in vertical direction. Note that the IC2 has the smallest eye box among the designed image combiners

Figure S22 shows the focus change experimental results in the optical bench prototype with IC2. Three real objects were used to show the focus change capability (a dinosaur doll - 250 cm, a lion doll - 80 cm and a police car - 30 cm). In the top three figures, the camera focus was changed from 250 cm to 30 cm while the system remained the same. Since the foveal display was located at the 80 cm plane, the defocus blurs were clearly shown in the close-up photos with the different camera focus. The bottom two figures shows the results when the foveal display was located at the camera focus plane. The results show that the foveal display provide high resolution inset image over 30 cm to 250 cm range. Whereas, the peripheral display image blur size was always the same regardless of camera focus as shown in the right close-up photos in Fig. S22. This results show the all-in-focus characteristics of the peripheral display system.

In overall, the Foveated AR optical bench prototype provided up to 60 cycles per degree high resolution inset for *pm*5 degrees circular FOV and 3 cycles per degree low resolution peripheral display for 85 degrees in horizontal and 78 degrees in vertical (101.4 degrees in diagonal) for 12 mm × 8 mm dynamic eye box at the 22 mm eye relief. The foveal display can provide the varifocal images from 30 cm to 250 cm and the peripheral display is all-in-focus.

C.4 Gaze Tracking

Estimating the gaze direction of the user wearing the foveated display glasses in real-time is implemented by extracting the pupil center extraction from the eye camera image followed by mapping the center position to a gaze vector. For pupil localization we use the network from Kim et al. [Kim et al. 2019] which has been proven to be fast and robust.

Remapping the pupil center to a gaze direction requires initial user calibration. The calibration step is implemented as follows. For a sequence of 5 gaze directions a gaze target is presented on the foveal display. The user is supposed to fixate the gaze target for each gaze direction. The foveal display is positioned with respect to an approximate gaze direction using a default gaze calibration. The observed monocular pupil positions during each gaze direction forms the basis for a user-specific polynomial calibration function mapping a 2d pupil position in camera image space to a monocular 2d gaze vector representing pitch and yaw components of the eye rotation in degrees. Although the pupil localization is very robust against reflections and lighting (see Fig.S23) we compensate for remaining slight estimation error during calibration by temporally averaging the pupil center positions over 10 estimated samples.

We do not estimate pupil size although it can be estimated from the pupil region. We also do not extract vergence information. A binocular version of the eye tracker can be used to compute vergence from both eyes. The vergence point would allow for automatic focus depth adaptation of the foveated display.

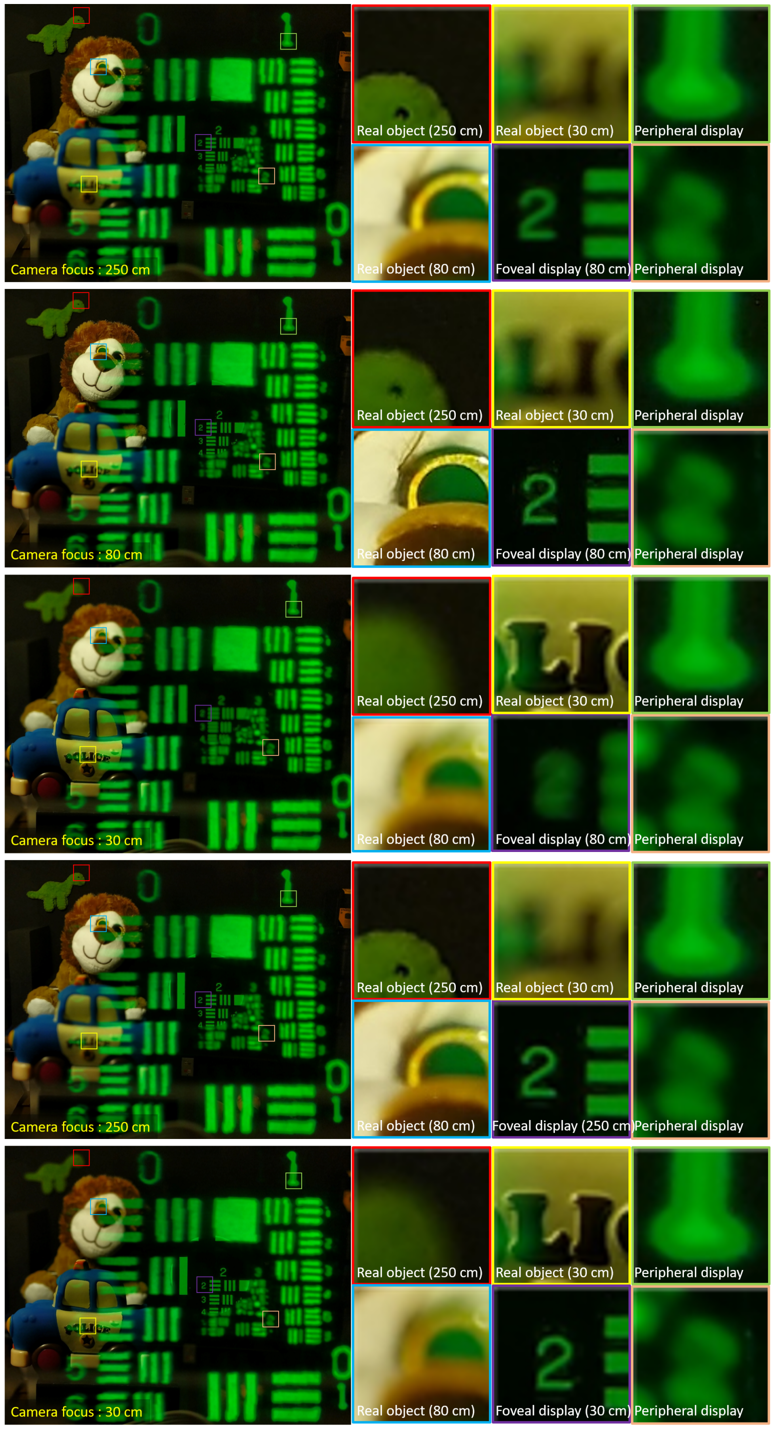

Fig. S22. Focus change experiment for optical bench prototype with IC2. The green dinosaur doll, the lion doll and the police car was located at 250 cm, 80 cm and 30 cm from the camera, respectively. The camera focus was change from 250 cm to 30 cm, and the foveal display plane was also changed from 250 cm to 30 cm. Note that the peripheral display is all-in-focus, providing similar blur size over the focus change.

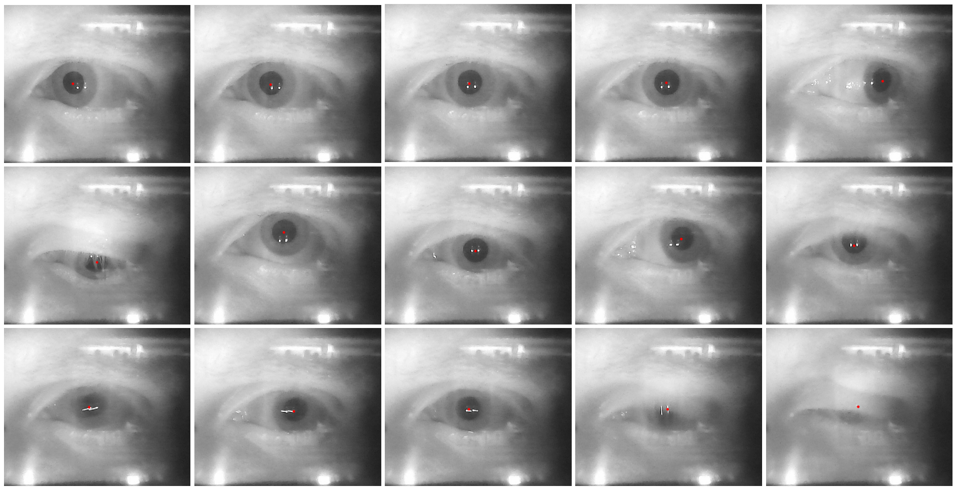

Fig. S23. On-axis Pupil Tracking. Top row : sequence of different gaze directions. Middle and bottom row: examples for high localization robustness in cases of partial pupil occlusion and significant motion blur during saccadic eye motions.

D WEARABLE PROTOTYPE

The detailed design and the components of the wearable prototype are shown in Fig. S24, S25, and S26.

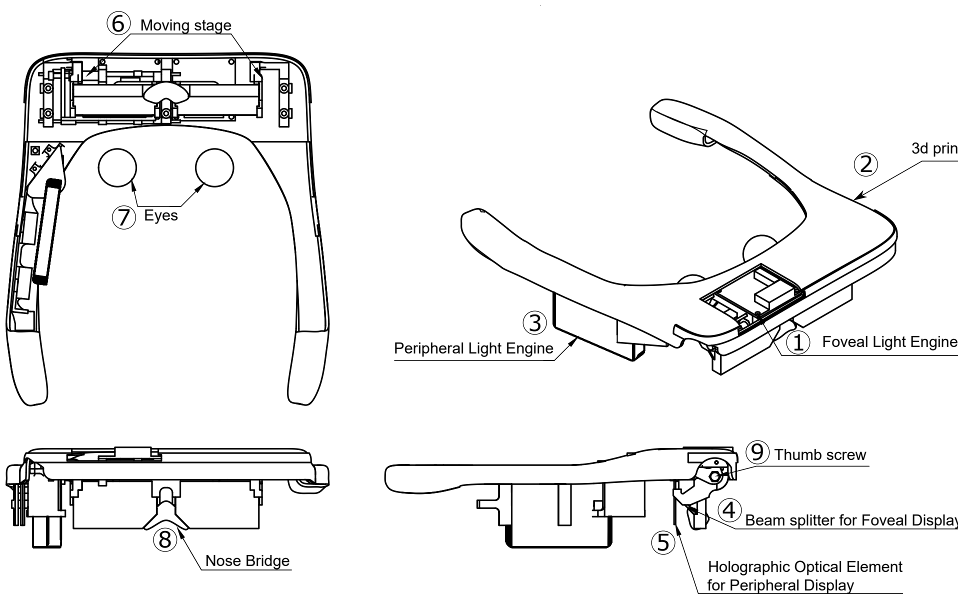

Fig. S24. Wearable Foveated Display Prototype

REFERENCES

P. Bernal-Molina, R. Montés-Micó, R. Legras, and N. López-Gil. 2014. Depth-of-field of the accommodating eye. *Optometry and Vision Science* 91, 10 (2014), 1208.

H. Huang and H. Hua. 2018. High-performance integral-imaging-based light field augmented reality display using freeform optics. *Optics Express* 26, 13 (2018), 17578–17590.

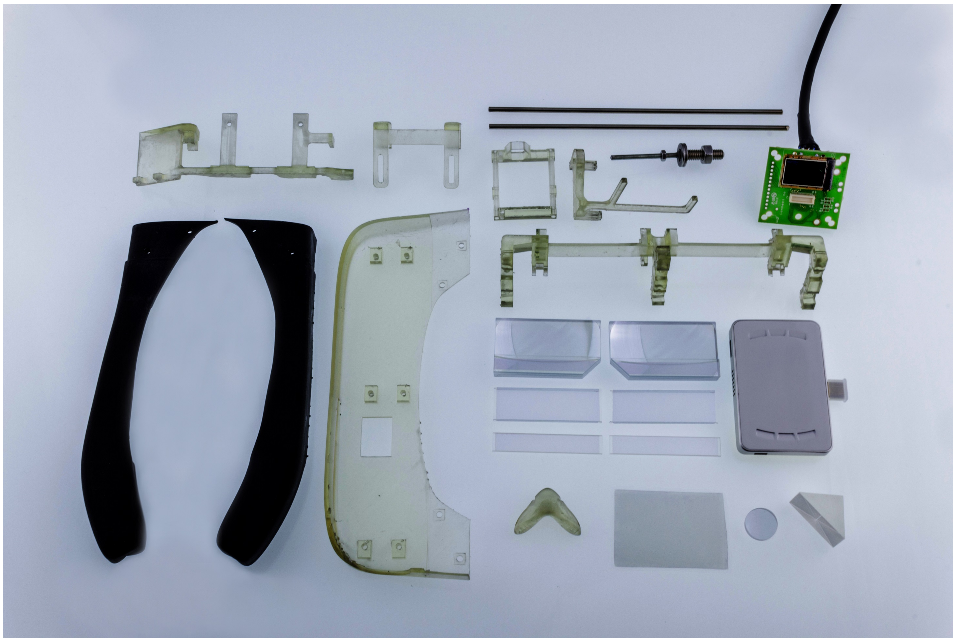

Fig. S25. Wearable prototype components

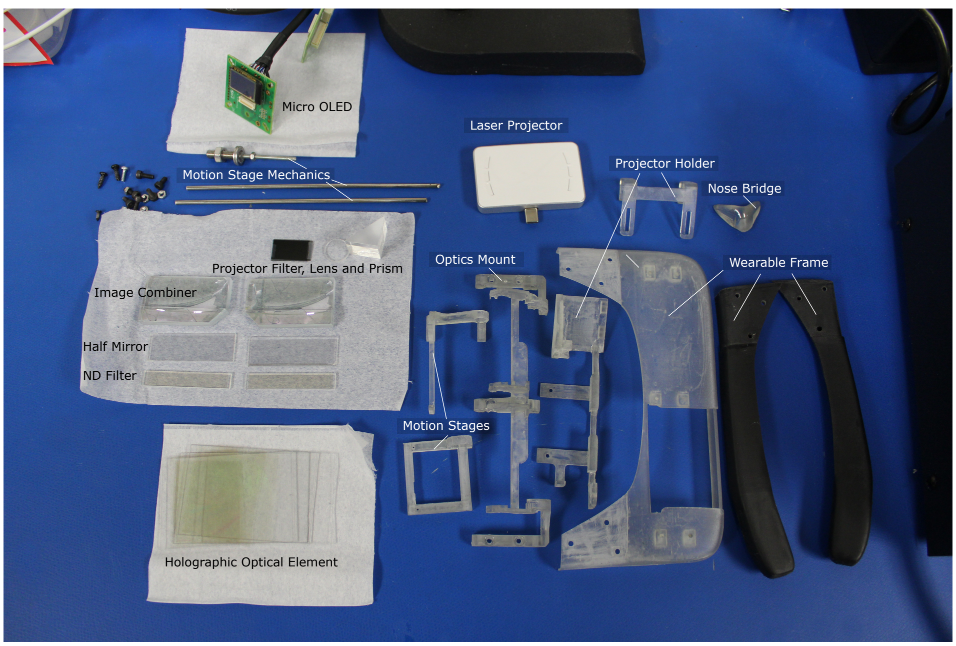

Fig. S26. Wearable prototype components ready for assembly

Changwon Jang, Kiseung Bang, Gang Li, and Byoungho Lee. 2018. Holographic Near-eye Display with Expanded Eye-box. *ACM Trans. Graph.* 37, 6, Article 195 (Dec. 2018), 14 pages. https://doi.org/10.1145/3272127.3275069

Changwon Jang, Kiseung Bang, Seokil Moon, Jonghyun Kim, Seungjae Lee, and Byoungho Lee. 2017. Retinal 3D: Augmented Reality Near-eye Display via Pupil-tracked Light Field Projection on Retina. *ACM Transactions on Graphics (TOG)* 36, 6 (Nov. 2017), 190:1–13. https://doi.org/10.1145/3130800.3130889

Joohwan Kim, Michael Stengel, Alexander Majercik, Shalini De Mello, Samuli Laine, Morgan McGuire, and David Luebke. 2019. NVGaze: Low-Latency, Near-Eye Gaze Estimation with an Anatomically-Informed Dataset. In *Proceedings of the SIGCHI Conference on Human Factors in Computing Systems (CHI '19)*. ACM, New York, NY, USA, 10.

Herwig Kogelnik. 1969. Coupled wave theory for thick hologram gratings. *Bell System Technical Journal* 48, 9 (1969), 2909–2947.

JJ Kulikowski and Peter Ewen King-Smith. 1973. Spatial arrangement of line, edge and grating detectors revealed by subthreshold summation. *Vision research* 13, 8 (1973), 1455–1478.

Dennis M Levi, Stanley A Klein, AP Aitsebaomo, et al. 1985. Vernier acuity, crowding and cortical magnification. *Vision research* 25, 7 (1985), 963–977.
Naoya Uchida. 1973. Calculation of diffraction efficiency in hologram gratings attenuated along the direction perpendicular to the grating vector. *JOSA* 63, 3 (1973), 280–287.